THE JOURNAL OF PHYSICAL CHEMISTRY Letters

pubs.acs.org/JPCL Letter

# Tuning Magnetism and Photocurrent in Mn-Doped Organic–Inorganic Perovskites

Lixia Ren, Yutao Wang, Min Wang, Shuanhu Wang, Yang Zhao, Claudio Cazorla, Changle Chen, Tom Wu,* and Kexin Jin*

Cite This: *J. Phys. Chem. Lett.* 2020, 11, 2577−2584 Read Online

ACCESS | Metrics & More | Article Recommendations | Supporting Information

**ABSTRACT:** Organic−inorganic perovskites have attracted increasing attention in recent years owing to their excellent optoelectronic properties and photovoltaic performance. In this work, the prototypical hybrid perovskite $CH_3NH_3PbI_3$ is turned into a ferromagnetic material by doping Mn, which enables simultaneous control of both charge and spin of electrons. The room-temperature ferromagnetism originates from the double exchange interaction between $Mn^{2+}$−$I^-$−$Mn^{3+}$ ions. Furthermore, it is discovered that the magnetic field can effectively modulate the photovoltaic properties of Mn-doped perovskite films. The photocurrent of Mn-doped perovskite solar cells increases by 0.5% under a magnetic field of 1 T, whereas the photocurrent of undoped perovskite decreases by 3.3%. These findings underscore the potential of Mn-doped perovskites as novel solution-processed ferromagnetic material and promote their application in multifunctional photoelectric-magnetic devices.

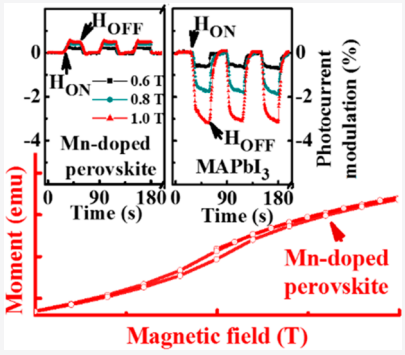


Methylammonium lead halide perovskites (particularly $CH_3NH_3PbI_3$, denoted as $MAPbI_3$) have received great attention because of their high absorption coefficient, long carrier lifetime and diffusion length, and desirable solar-matching optical bandgap.[1−5] $MAPbI_3$ and its variants have been used to fabricate highly efficient perovskite solar cells (PSC), tunable light-emitting diodes and high-sensitive photodetectors.[6−8] In recent years, the certified power conversion efficiency of PSC has reached 25.2%.[9−11] However, so far perovskite-based devices have mainly exploited the electrons in the materials, and it remains a challenging task to realize multifunctional properties in perovskite films.

Particularly, manipulating magnetism in semiconductors is the foundation of spintronics.[12−14] As nonmagnetic materials, hybrid perovskites were recently integrated into spintronic devices and used as a spacer between ferromagnetic (FM) electrodes.[15−19] It was reported that the magnetic field can assist the preparation of perovskite films, enhancing the performance of PSC.[19] Moreover, the magnetic field effect is significant in perovskites because of the strong spin−orbit coupling (SOC) brought by the heavy atoms (Pb, I) in their building block.[20,21] In a recent work, Zhang et al. attributed the influence of magnetic field on photoelectric characteristics to the spin-mixing of photogenerated electron−hole pairs with different *g*-factors.[20] However, it is important to note that all the research efforts have focused on investigating perovskites as semiconductors, and it remains an open question if robust magnetism can be introduced into hybrid perovskites via doping or other means.

FM semiconductors have attracted unprecedented attention because of the advancement of microelectronic and high-frequency recording devices. Some materials, such as GaN, GaAs, ZnO, and $SnO_2$, can be turned into FM by introducing Mn or other appropriate transition metal ions.[22−25] The origin of FM in the doped semiconductors is under intense discussion, and the proposed mechanisms include Ruderman−Kittel−Kasuya−Yosida (RKKY) model,[26,27] superexchange interaction, and double-exchange interaction.[28,29] For the hybrid perovskites, Mn is a promising dopant owing to its large net magnetic moment and isoelectronic structure to $Pb^{2+}$ in the host lattice. For instance, Williams et al. realized a new class of organic−inorganic perovskites by doping Mn, Fe, Co, and Ni during the growth of $MAPbI_3$ films.[30] Klug et al. reported that partial substitution of Pb by divalent metals including Mn would influence the photovoltaic and optical performances of $MAPbI_3$ films.[31] Náfrádi et al. synthesized magnetic perovskite $MA(Mn:Pb)I_3$ single crystals, which show a Curie temperature of 25 K.[32] In the work by Cai et al., lead-free double perovskites ($Cs_2GeMX_6$, transition metal M = V, Mn, or Ni; X = Cl, Br, or I) have been achieved showing high Curie temperatures.[33] Moreover, Mn element can present multiple valence states, such as $Mn^{2+}$, $Mn^{3+}$, $Mn^{4+}$, and $Mn^{7+}$, to trigger unique physical properties. Therefore, Mn-doped organic−inorganic perovskites are very promising in the

**Received:** January 5, 2020
**Accepted:** March 12, 2020
**Published:** March 12, 2020






https://dx.doi.org/10.1021/acs.jpclett.0c00034
*J. Phys. Chem. Lett.* 2020, 11, 2577−2584

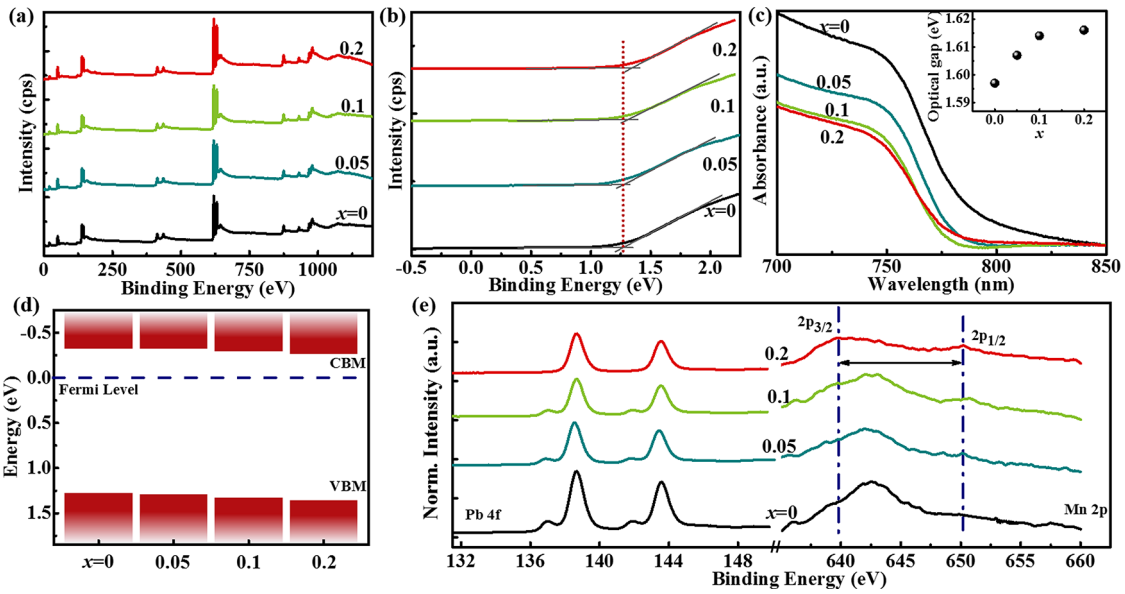


**Figure 1.** (a, b) Full XPS spectra and the valence band spectra of the films. (c, d) UV−visible absorption spectra and the band diagrams of the films, respectively. Here, CBM is determined by adding the optical bandgap to VBM. The inset of panel c shows the optical bandgap as a function of $x$. (e) XPS spectra of Pb 4f and Mn 2p for the set of samples.

development of multifunctional devices, and it is an urgent task to investigate their physical properties with the aim of integrating such films in spintronic devices.

In this work, $MAPb_{1-x}Mn_xI_3$ ($x$ is the molar ratio and $x$ = 0, 0.05, 0.1, and 0.2) films were deposited on glass substrates via solution processing. The doped films exhibit robust FM properties at room temperature. Further, the photoelectric and photovoltaic performances of perovskite films can be modulated by the magnetic field. Intriguingly, we found that the magnetic field can effectively decrease the photoresistance of Mn-doped films as well as increase the photocurrent of Mn-doped PSC. These findings present a new perspective of doped perovskite films as a promising building block in magnetic and spintronic devices.

The energy band of perovskite films was characterized by X-ray photoemission spectroscopy (XPS) and UV−visible absorption measurements. The full XPS spectra of Mn-doped perovskite films are shown in Figure 1a, and no new peak was observed with increasing $x$. The valence-band maximum (VBM, $E_F - E_{VBM}$, where $E_F$ = 0 eV) is obtained from the edge of valence band spectra, as shown in Figure 1b.[34] The VBM of perovskite films increases from 1.27 to 1.35 eV with increasing $x$. The optical bandgap, calculated from the edge of UV−visible absorption spectra, also increases slightly from 1.59 to 1.61 eV (Figure 1c). The Tauc plot method is used to deduce the optical bandgap (for details, see Figure S1). Adding the optical bandgap to the VBM, the conduction-band minimum (CBM, $E_F - E_{CBM}$) is calculated and shown in Figure 1d.[35] With increasing $x$, the VBM shifts away from the Fermi level while the CBM gets closer. In fact, there are significant energy level differences between the empty 4s, 4p orbitals of Mn and the empty 6s, 6p orbitals of Pb. The upper edge of valence band is constituted mainly by halogen p orbitals interacting with Pb s orbitals in perovskites, whereas the Pb p orbitals contribute to the lower edge of conduction band.[36] Thus, the shift of VBM and CBM derives from the influence of Mn doping.

In addition, the change in areas for core level peaks (Pb 4f, Mn 2p) is consistent with the doping ratio (Figure 1e). We did not estimate the Mn doping concentration from the XPS data because of the strong surface effect that stems from the different nucleation rates of the perovskite and unreacted Mn precursors.[37] Instead, the atomic ratio of Mn: Pb in films was calculated by using the energy dispersive spectroscopy (EDS) measurements carried out in a scanning electron microscope on fresh perovskite films. As summarized in Table 1, the slight

**Table 1. Mn:Pb Atomic Ratios Obtained from the EDS data**

| $x$ | 0 | 0.05 | 0.10 | 0.20 |
|---|---|---|---|---|
| Mn:Pb | 0:1 | 0.09:1 | 0.16:1 | 0.29:1 |

deviations of experimentally derived compositions may come from the accumulation of unreacted Mn precursors on the film surfaces. Nevertheless, the Mn:Pb ratios largely follow the trend of stoichiometry expected for the doped films.

To investigate the Mn-doped effect on $MAPbI_3$ films, the evolution of structure as a function of $x$ was characterized by using X-ray diffraction (XRD). As shown in Figure 2a, the XRD patterns indicate the typical tetragonal phase in the

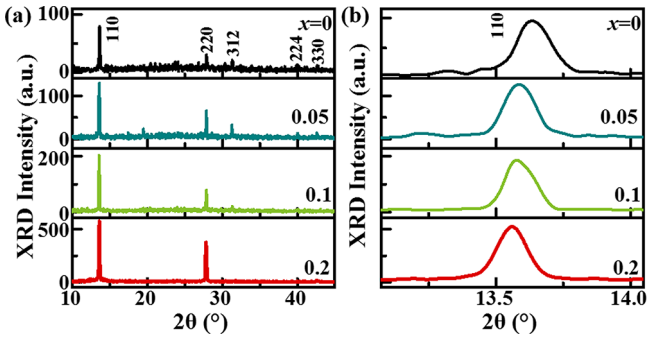


**Figure 2.** (a) XRD pattern of the $MAPb_{1-x}Mn_xI_3$ films. (b) The amplified XRD spectra of perovskite films.


https://dx.doi.org/10.1021/acs.jpclett.0c00034
J. Phys. Chem. Lett. 2020, 11, 2577−2584

$MAPbI_3$ film and no secondary phase was detected. With increasing $x$, the intensity of (110) characteristic peak for $MAPbI_3$ gradually increases. In addition, it is observed that the (110) peak position is shifted to lower angles with increased $x$, as shown in Figure 2b, which indicates a slight increase of the spacing between (110) crystal planes. It is known that the ionic radii of $Mn^{2+}$ and $Mn^{3+}$ are smaller than that of $Pb^{2+}$, from which the crystal plane spacing should decrease if Mn substitute Pb in the perovskite lattice. Since this is contradictory to the results of XRD measurement, some Mn ions may be doped as interstitials in the perovskite film. In such solution-processed perovskite films with very soft lattice, doped Mn ions may be located in a variety of positions in the lattice and create charged defects in grain boundaries, which is different from the diluted magnetic semiconductors grown by vapor-based techniques like molecular beam epitaxy.[38,39] It is noteworthy that the film with $x = 0.2$ shows only (110) and (220) diffraction peaks, demonstrating a highly textured nature.

It has been concluded that the morphology is crucial for improving performances in optoelectronic and photovoltaic devices from previous studies.[40] Scanning electron microscope (SEM) is used to characterize the morphology of samples. As shown in Figure 3, the Mn-dopant has indeed a strong influence on the morphology of $MAPbI_3$ films, and the grain size increases from 100−200 nm at $x = 0$ to 500−700 nm at $x = 0.2$. We thus decided to focus the magnetic measurements on the film with $x = 0.2$.

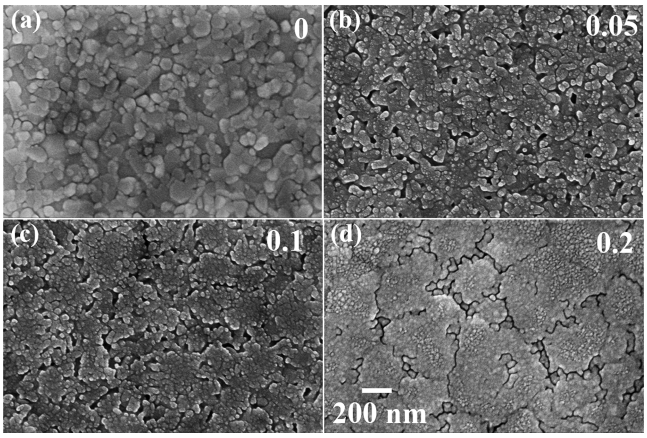


**Figure 3.** Top-view SEM images of the $MAPb_{1-x}Mn_xI_3$ films.

We checked the magnetic properties of Mn-doped and undoped $MAPbI_3$ using the superconducting quantum interference device (SQUID). As shown in Figure 4a, the magnetic moment as a function of the magnetic field ($M-H$) for the film with $x = 0.2$ is characterized at 300 K. To avoid the influence from substrates, powder sample with a weight of 6.64 mg was obtained by scraping the film with a nonmagnetic plastic tweezer. The nonlinear $M-H$ behavior illustrates the appearance of FM magnetization in the Mn-doped perovskite. As shown in Figure 4b, we found a clear coercive field of about 50 Oe for the Mn-doped $MAPbI_3$ sample. The undoped perovskite, on the other hand, is diamagnetic, as shown in Figure 4a. Clearly, the magnetic property of the doped perovskite polycrystal film can be attributed to the influence of Mn dopant. This result excludes the superexchange as the dominant magnetic interaction since it is exclusively used to explain the origin of antiferromagnetism in insulators.[28,41] Furthermore, the RKKY interaction which underpins the theory of giant magnetoresistance (GMR) is not favorable here either[42,43] because the carrier density of hybrid perovskites is known to be rather low and not sufficient to sustain the spin coupling between electrons in d orbitals.[44,45] It is noted that the room-temperature FM observed herein differs from the previous report on the existence of FM at cryogenic temperatures in Mn-doped perovskite single crystal,[32] which may be ascribed to the different structural orders and defect concentrations between single crystal and polycrystal film samples.[46]

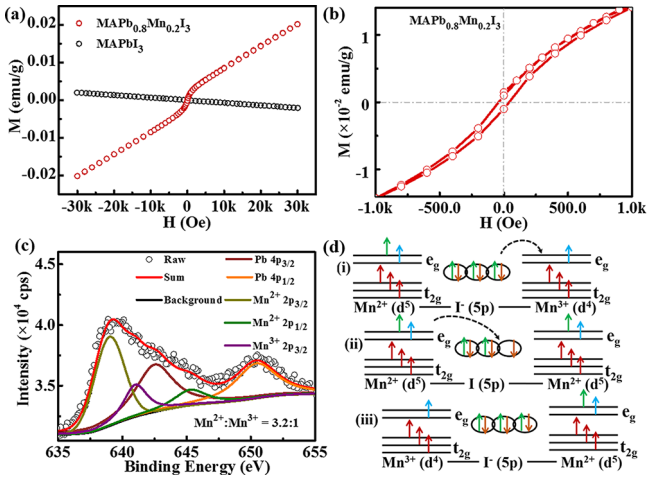


**Figure 4.** (a) $M-H$ curve of $MAPb_{0.8}Mn_{0.2}I_3$ measured at 300 K. The data of the undoped counterpart are also shown for comparison. (b) Magnetization data in the low-field regime showing the ferromagnetic hysteresis loop. (c) Mn 2p XPS peaks of the $MAPb_{0.8}Mn_{0.2}I_3$ film. (d) Schematic of the double-exchange interaction between Mn and I ions.

To explain the appearance of FM property, the alternation of Mn valence in the doped perovskite should be taken into consideration. As shown in Figure 4c, Mn ions oxidation state can be determined by the XPS measurements.[47−51] The Mn 2p spectrum of doped perovskite with $x = 0.2$ is fitted to achieve the quantification of $Mn^{2+}$ and $Mn^{3+}$. It should be noted that the fraction of $Mn^{4+}$ appears to be negligible, which is different from mixed-valence oxide manganites.[52,53] The fitting results are summarized in Table S1. From the XPS data, the $Mn^{2+}/Mn^{3+}$ ratio is determined to be 3.2:1. The likely presence of $Mn^{2+}-I^{-}-Mn^{3+}$ motifs in the sample suggests a plausible explanation for the ferromagnetic coupling observed between Mn ions (Figure 4d), that is, the double exchange mechanism proposed by Zener for analogous oxide perovskites.[29,54] Here, Mn ions are coordinated to I ions in the perovskite structure, and a crystal field splits the 3d orbitals into $e_g$ and $t_{2g}$. In the $Mn^{3+}$ ions, three out of the four electrons occupy the $t_{2g}$ level and the remaining one the $e_g$ level; in the $Mn^{2+}$ ions, three out of five electrons occupy the $t_{2g}$ level and the remaining two the $e_g$ level. All spins are parallelly aligned to satisfy the Hund's rules.[55] The $I^-$ ions provide a closed shell to transfer electrons.[29] In the $Mn^{2+}-I^{-}-Mn^{3+}$ motif, the $I^-$ ion may transfer one spin-up electron to the $Mn^{3+}$ ion and the resulting empty state can be subsequently filled by one electron from the $Mn^{2+}$ ion. Accordingly, the ionic configuration changes from $Mn^{2+}-I^{-}-Mn^{3+}$ ($\psi_1$) to $Mn^{3+}-I^{-}-Mn^{2+}$ ($\psi_2$), which represents two degenerate states involving electron delocalization (in the crystal, such a degeneracy is typically lifted by the


https://dx.doi.org/10.1021/acs.jpclett.0c00034
J. Phys. Chem. Lett. 2020, 11, 2577−2584

local environment). The electron transfer from $Mn^{2+}$ to $Mn^{3+}$ mediated by $I^-$ is possible only if the two Mn ions are coupled ferromagnetically since the spin of the electron cannot change during the hopping processes and Hund's rules need to be satisfied (Figure 4d). We should note that only a small fraction of Mn ions is expected to exhibit ferromagnetism through double exchange with I ions, and the majority may be locally coupled in antiferromagnetic interaction or left as isolated spins. Future X-ray magnetic circular dichroism experiments may help shed light on the mechanism of magnetism and the nature of magnetic interactions in such doped hybrid films.[56]

Considering the magnetic nature of $MAPb_{0.8}Mn_{0.2}I_3$, we measured the magnetic field effect on the photoelectric performance. First, the quality of the $MAPbI_3$ film was confirmed by the performance of a solar cell, in which an efficiency of 15.1% was obtained (Figure 5). In addition, the solar cell with the Mn dopant exhibits an undesirable S-shaped $J-V$ curve, which may origin from the decreased carrier mobility of the Mn-doped solar cell,[57] resulting in a low PCE because of a significantly reduced fill factor, which agrees with the previous report.[29]

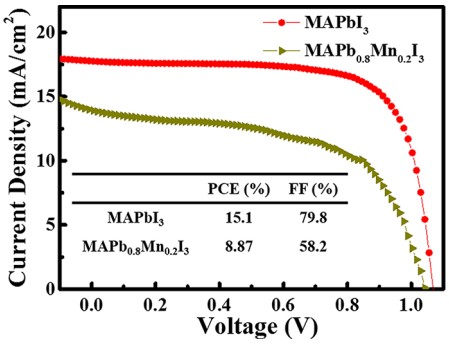


**Figure 5.** Current−voltage ($J-V$) characteristic scans measure from the solar cells. The inset shows the power conversion efficiency (PCE) and the fill factor (FF) of solar cells.

The schematic diagram of the photovoltaic device structure is shown in Figure 6a. As shown in Figure 6b, the photocurrent, $I_P$, is sensitive to the magnetic field. Here, we define the relative change of short-circuit photocurrent as $MI_P$ ($MI_P = \frac{I_P(H) - I_P(0)}{I_P(0)} \times 100\%$, where $I_P(H)$ is photocurrent under the magnetic field). For the PSC based on $MAPb_{0.8}Mn_{0.2}I_3$, the increasing magnetic field induces an upsurge in $MI_P$. Under the applied magnetic field of 1 T, the value of $MI_P$ in Mn-doped PSC is about 0.5%, while that of the undoped PSC is −3.3%. The magnetic field dependence of $MI_P$ for the Mn-doped and the undoped samples is summarized in Figure 6c. Clearly, the magnetic field induces opposite trend of changes in the photocurrents of Mn-doped and undoped perovskites. We also characterized the magnetic-field-induced modulation of photoresistance (noted as $R_P$, at a 10 V bias) for the films, and the schematic diagram is shown in Figure 6d. As shown in Figure 6e, the $R_P$ of $MAPb_{0.8}Mn_{0.2}I_3$ film decreases with increasing magnetic field. In contrast, the $R_P$ of undoped film increases with increasing magnetic field. The relative change of $R_P$ (noted as $MR_P$, and $MR_P = \frac{R_P(H) - R_P(0)}{R_P(0)} \times 100\%$, where $R_P(H)$ is photoresistance under magnetic field) is summarized in Figure 6f. Under the magnetic field of 1 T, the $MR_P$ values of Mn-doped and undoped films are −3.3% and 7.0%, respectively.

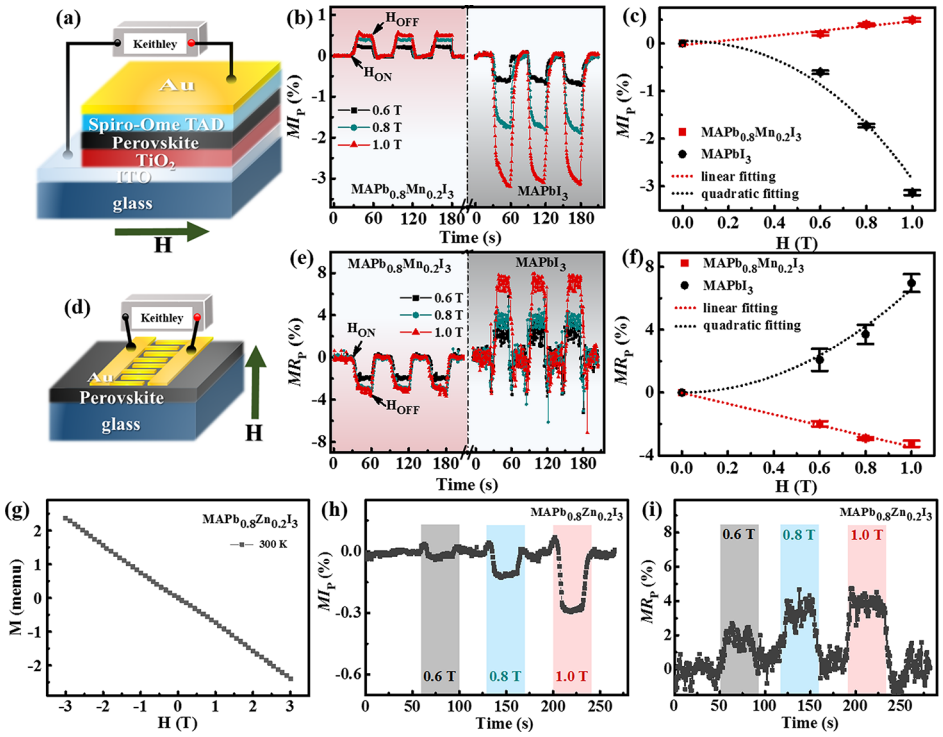


**Figure 6.** (a) Schematic diagram of architecture and measurement for PSCs. (b) $MI_P$ for PSCs as a function of time. $H_{ON}$ and $H_{OFF}$ are the on and off state of the magnetic field. (c) $MI_P$ as a function of the magnetic field. Error bar is given and the imaginary line represents the fitted results. (d) Schematic diagram of architecture and measurement for films. (e, f) $MR_P$ for films as a function of time and magnetic field, respectively. (g) $M-H$ curve of $MAPb_{0.8}Zn_{0.2}I_3$ measured at 300 K. (h) $MI_P$ and (i) $MR_P$ data for the $MAPb_{0.8}Zn_{0.2}I_3$ sample.


https://dx.doi.org/10.1021/acs.jpclett.0c00034
J. Phys. Chem. Lett. 2020, 11, 2577−2584

It is clear that both $MI_P$ and $MR_P$ of the $MAPb_{0.8}Mn_{0.2}I_3$ film vary linearly with the magnetic field. Application of a magnetic field aligns the spins of the Mn ions and strengthens the $d^5-e_g$ double exchange, thus enhancing the electron hopping and resulting in a decrease of photoresistance.[58,59] In contrast, $MI_P$ and $MR_P$ of the undoped perovskite change nonlinearly (quadratic dependence) with the magnetic field. The magnetic field effect in the undoped perovskite films may be related to the Lorentz force and similar to the ordinary magnetoresistance found in conventional diamagnetic materials.[59] An electric field, either built-in or external, can induce the directional migration of photogenerated carriers. When the magnetic field is perpendicular to the direction of motion of these carriers, the Lorentz force extends the motion path of photogenerated carriers to enhance the carrier recombination, leading to a nonlinear increase (decrease) in $MR_P$ ($MI_P$). Other factors like inhomogeneous charge transport and device configuration may also contribute to the positive magnetoresistance in the undoped perovskite films,[60] and more characterizations should be carried out to reveal the underlying mechanism.

As a control experiment, we also prepared a Zn-doped perovskite film and investigated its magnetic properties. As shown in Figure 5g, the magnetic moment of the $MAPb_{0.8}Zn_{0.2}I_3$ film as a function of the magnetic field indicates that the Zn-doped perovskite is diamagnetic. In addition, we measured the relative changes of $R_P$ and $I_P$ for the Zn-doped perovskite film under varied magnetic field (Figure 6h and 6i). Under a magnetic field of 1 T, the $MI_P$ and $MR_P$ values of Zn doped perovskites are −0.3% and 3.9%, respectively. The quadratic dependence of $MI_P$ and $MR_P$ on the magnetic field is shown in Figure S2, which is consistent with its diamagnetic nature. These results suggest that a proper doping element should be selected to render a ferromagnetic perovskite film.

In conclusion, we observed the emergence of magnetism in Mn-doped $MAPbI_3$ at room temperature and investigated its effect on the photoelectric properties. This ferromagnetism stems from the double-exchange mechanism taking place in the $Mn^{2+}-I^{-}-Mn^{3+}$ framework. Owing to the new Mn-endowed magnetic degree of freedom, the application of a magnetic field can effectively modulate the photovoltaic and photo-electric performance in the hybrid perovskites, which may have implications for a wide range of optoelectronic devices. In particular, a magnetic field of 1 T induces an increase of photocurrent of 0.5% in Mn-doped $MAPbI_3$, whereas the photocurrent of the undoped counterpart decreases by 3.3%. Our findings suggest that a magnetic field can be used as an additional tuning parameter for optimizing the performance of photovoltaic materials, thus promoting the implementation of doped hybrid perovskites in multifunctional devices. Furthermore, since SOC is strong in perovskites because of the heavy ions (e.g., Pb, I), the related effect, such as Rashba splitting may be modulated by the Mn doping, which warrants future investigations.

## ■ EXPERIMENTAL METHODS

*Perovskite Film Preparation.* Glass substrates were cleaned with detergent solution, deionized water, isopropanol, and absolute ethyl alcohol with 15 min of sonication for each step and finally transferred to argon-filled compact plasma sputtering coater for 40 min. Then, the substrates were transferred to an $N_2$-filled glovebox. Methylammonium iodide ($CH_3NH_3I$, MAI), lead acetate trihydrate ($Pb(CH_3CO_2)_2{\cdot}3H_2O$ or $PbAc_2{\cdot}3H_2O$), and manganous acetate tetrahydrate ($Mn(CH_3CO_2)_2{\cdot}4H_2O$ or $MnAc_2{\cdot}4H_2O$) were purchased from Xi'an Polymer Light Technology, Corp. $MnAc_2{\cdot}4H_2O$ is soluble in dimethylformamide. Moreover, one-step method for preparing perovskite films can preserve Mn element in perovskite films. MAI (0.6 mmol) was dissolved in 0.2 mL of anhydrous *N*,*N*-dimethylformamide (DMF) and then added to 0.2 mmol mixture of $PbAc_2{\cdot}3H_2O$ and $MnAc_2{\cdot}4H_2O$ ($0 \leq Mn/(Pb + Mn) \leq 0.2$), depending on the desired concentration, thus obtaining precursor solution ($MAPb_{1-x}Mn_xI_3$ is 1 M). The perovskite films were prepared by spin-coating precursor solution at 6000 rpm on glass substrates and the films were annealed at 100 °C for 5 min.

*Device Fabrication.* The solar cells employed a device structure of glass/FTO/$TiO_2$/perovskite/spiro-MeOTAD/Au. FTO substrates were exposed to a UV-ozone environment for 5 min. A thin $TiO_2$ compact layer was deposited on a cleaned FTO substrate by spin-coating using a solution composed of 0.3 M titanium diisopropoxide bis(acetylacetonate) (75 wt % in 2-propanol, Sigma-Aldrich) in 2-propanol (99.9% Sigma-Aldrich) at 4000 rpm for 30 s. The coated FTO substrate was then dried at 120 °C for 5 min, followed by calcination at 500 °C for 30 min. After it was cooled to ambient temperature, a $TiO_2$ paste (30-TS, G24 power Ltd., UK) diluted in ethanol was spin-coated on the compact $TiO_2$-coated FTO substrate at 6000 rpm for 30 s to form a mesoporous $TiO_2$ film. After coating, the bilayer was dried at 120 °C for 5 min and then sintered at 500 °C for 30 min again. Prior to perovskite layer preparation, the bilayer $TiO_2$ film was treated in a 40 mM $TiCl_4$ solution at 70 °C for 30 min. After it was rinsed with deionized water and ethanol sequentially, the film was dried in air and resintered at 450 °C for 30 min. After the as-prepared FTO/bilayer $TiO_2$/perovskite film cooled down from annealing, a layer of spiro-OMe TAD was spin-coated on the top at 4000 rpm for 30 s. The spiro-MeOTAD solution was composed of 75 mM 2,20,7,70-tetrakis(*N*,*N*-di-4-methoxyphenylamino)-9,90-spirobifluorene (spiro-OMeTAD, > 99%, Lumtec, Taiwan), 35 mM lithium bis(trifluoromethyl sulphonyl)imide (Li-TFSI, 99.95%, Sigma-Aldrich), and 120 mM *tert*-butylpyridine (tBP, > 96%, Sigma-Aldrich) in chlorobenzene (99.8%, Sigma-Aldrich). Li-TFSI was dissolved in acetonitrile (99.5%, Merck) at a concentration of 340 mg/mL. Finally, a gold electrode was deposited on top of the spiro-MeOTAD layer by thermal evaporation. The entire fabrication process was conducted in a controlled environment with a relative humidity level in the range of 30−45% and a temperature of approximately 25 °C. Au electrodes for the transport measurement were deposited on the surface of $MAPbI_3$ films using a sputtering coater.

*Measurements.* X-ray diffraction (XRD) was performed using an X-ray diffractometer (XRD-7000, Shimadzu) with a Cu K$\alpha$ radiation source ($\lambda$ = 1.5406 Å) at a step size of 0.02°. The surface morphology of thin films was characterized by using a scanning electron microscope (SEM, JSM-6700F, JEOL). The ultraviolet−visible (UV−vis) absorption spectrum was measured using an ultraviolet−visible spectrophotometer (U-3010, Hitachi). The energy dispersive spectrometer (EDS, Oxford INCA) was used to obtain the content of the elements. X-ray photoemission spectra (XPS) were measured using monochromated Al K$\alpha$ radiation (1486.7 eV) at a resolution of 400 meV. The superconducting quantum interference device (SQUID, MPMS-XL-7) was used to characterize the magnetic


https://dx.doi.org/10.1021/acs.jpclett.0c00034
J. Phys. Chem. Lett. 2020, 11, 2577−2584

properties. The photoelectric and photovoltaic performance of samples were measured using a low-noise probe station and a current−voltage source (6487 Keithley multimeter).

## ■ ASSOCIATED CONTENT

### Supporting Information

The Supporting Information is available free of charge at https://pubs.acs.org/doi/10.1021/acs.jpclett.0c00034.

Detailed calculation of band gap for samples, the changed $MI_P$ and $MR_P$ of Zn doped $MAPbI_3$, and the fitted result of Mn 2p XPS peaks (PDF)

## ■ AUTHOR INFORMATION


### Corresponding Authors

**Tom Wu** − *School of Materials Science and Engineering, University of New South Wales, Kensington, New South Wales 2052, Australia;* orcid.org/0000-0003-0845-4827; Email: tom.wu@unsw.edu.au

**Kexin Jin** − *Shaanxi Key Laboratory of Condensed Matter Structures and Properties, School of Science, Northwestern Polytechnical University, Xi'an 710072, China;* orcid.org/0000-0001-5838-0315; Email: jinkx@nwpu.edu.cn

### Authors

**Lixia Ren** − *Shaanxi Key Laboratory of Condensed Matter Structures and Properties, School of Science, Northwestern Polytechnical University, Xi'an 710072, China*

**Yutao Wang** − *School of Materials Science and Engineering, University of New South Wales, Kensington, New South Wales 2052, Australia*

**Min Wang** − *Shaanxi Key Laboratory of Condensed Matter Structures and Properties, School of Science, Northwestern Polytechnical University, Xi'an 710072, China*

**Shuanhu Wang** − *Shaanxi Key Laboratory of Condensed Matter Structures and Properties, School of Science, Northwestern Polytechnical University, Xi'an 710072, China;* orcid.org/0000-0002-5386-1037

**Yang Zhao** − *Shaanxi Key Laboratory of Condensed Matter Structures and Properties, School of Science, Northwestern Polytechnical University, Xi'an 710072, China*

**Claudio Cazorla** − *School of Materials Science and Engineering, University of New South Wales, Kensington, New South Wales 2052, Australia;* orcid.org/0000-0002-6501-4513

**Changle Chen** − *Shaanxi Key Laboratory of Condensed Matter Structures and Properties, School of Science, Northwestern Polytechnical University, Xi'an 710072, China*

Complete contact information is available at: https://pubs.acs.org/10.1021/acs.jpclett.0c00034


### Notes

The authors declare no competing financial interest.

## ■ ACKNOWLEDGMENTS

This work was supported by the National Natural Science Foundation of China (Nos. 51572222, 61601367, and 11604265), the Fundamental Research Funds for Central Universities (Grant 3102016ZY028) and Australian Research Council (DP190103316). L.X.R. would like to thank Peng Zhai for discussion and technical assistance and Xiaodong Zhang and Fan Xu for experimental assistance.

## ■ REFERENCES


(1) Yang, W. S.; Park, B. W.; Jung, E. H.; Jeon, N. J.; Kim, Y. C.; Lee, D. U.; Shin, S. S.; Seo, J.; Kim, E. K.; Noh, J. H.; et al. Iodide Management in Formamidinium-Lead-Halide-Based Perovskite Layers for Efficient Solar Cells. *Science* **2017**, *356*, 1376−1379.

(2) Zhang, Z.; Wang, M.; Ren, L.; Jin, K. Tunability of Band Gap and Photoluminescence in $CH_3NH_3PbI_3$ Films by Anodized Aluminum Oxide Templates. *Sci. Rep.* **2017**, *7*, 1918.

(3) Ma, C.; Shi, Y.; Hu, W.; Chiu, M. H.; Liu, Z.; Bera, A.; Li, F.; Wang, H.; Li, L. J.; Wu, T. Heterostructured $WS_2/CH_3NH_3PbI_3$ Photoconductors with Suppressed Dark Current and Enhanced Photodetectivity. *Adv. Mater.* **2016**, *28*, 3683−3689.

(4) Niu, T.; Lu, J.; Munir, R.; Li, J.; Barrit, D.; Zhang, X.; Hu, H.; Yang, Z.; Amassian, A.; Zhao, K.; et al. Stable High-Performance Perovskite Solar Cells via Grain Boundary Passivation. *Adv. Mater.* **2018**, *30*, 1706576.

(5) Lee, M. M.; Teuscher, J.; Miyasaka, T.; Murakami, T. N.; Snaith, H. J. Efficient Hybrid Solar Cells Based on Meso-Superstructured Organometal Halide Perovskites. *Science* **2012**, *338*, 643−647.

(6) Li, H.; Shi, W.; Huang, W.; Yao, E. P.; Han, J.; Chen, Z.; Liu, S.; Shen, Y.; Wang, M.; Yang, Y. Carbon Quantum Dots/$TiO_x$ Electron Transport Layer Boosts Efficiency of Planar Heterojunction Perovskite Solar Cells to 19. *Nano Lett.* **2017**, *17*, 2328.

(7) Tan, Z. K.; Moghaddam, R. S.; Lai, M. L.; Docampo, P.; Higler, R.; Deschler, F.; Price, M.; Sadhanala, A.; Pazos, L. M.; Credgington, D.; et al. Bright Light-Emitting Diodes Based on Organometal Halide Perovskite. *Nat. Nanotechnol.* **2014**, *9*, 687.

(8) Ren, L.; Wang, M.; Wang, S.; Zhang, Z.; Jin, K. Enhanced Photoresponsive Properties of Perovskite Films on Metal Oxide $LaAlO_3$ Substrates. *J. Phys. Chem. C* **2018**, *122*, 10495−10500.

(9) Giordano, F.; Abate, A.; Correa Baena, J. P.; Saliba, M.; Matsui, T.; Im, S. H.; Zakeeruddin, S. M.; Nazeeruddin, M. K.; Hagfeldt, A.; Graetzel, M. Enhanced Electronic Properties in Mesoporous $TiO_2$ via Lithium Doping for High-Efficiency Perovskite Solar Cells. *Nat. Commun.* **2016**, *7*, 10379.

(10) Mazzarella, L.; Lin, Y. H.; Kirner, S.; Morales-Vilches, A. B.; Korte, L.; Albrecht, S.; Crossland, E.; Stannowski, B.; Case, C.; Snaith, H. J.; Schlatmann, R. Infrared Light Management Using a Nanocrystalline Silicon Oxide Interlayer in Monolithic Perovskite/Silicon Heterojunction Tandem Solar Cells with Efficiency above 25%. *Adv. Energy Mater.* **2019**, *9*, 1803241.

(11) *NREL Efficiency Chart*. https://www.nrel.gov/pv/cell-efficiency.html (accessed October 2019).

(12) Li, W.; Yan, H.; Chai, X. J.; Wang, S. H.; Dong, X. L.; Ren, L. X.; Chen, C. L.; Jin, K. X. Modulation of persistent magnetoresistance by piezo-strain effect in Manganite-based heterostructures. *Appl. Phys. Lett.* **2017**, *110*, 192411.

(13) Yan, H.; Zhang, Z.; Wang, S.; Wei, X.; Chen, C.; Jin, K. Magnetism Control by Doping in $LaAlO_3/SrTiO_3$ Heterointerfaces. *ACS Appl. Mater. Interfaces* **2018**, *10*, 14209−14213.

(14) Pei, H.; Guo, S.; Yan, H.; Chen, C.; Luo, B.; Jin, K. Enhanced Magneto-Electric Effect in Manganite Tricolor Superlattice with Artificially Broken Symmetry. *Chin. Phys. B* **2018**, *27*, No. 097701.

(15) Xu, Q.; Liu, E.; Qin, S.; Shi, S.; Shen, K.; Xu, M.; Zhai, Y.; Dong, S. Spin Transport in $CH_3NH_3PbI_3$. *J. Phys. D: Appl. Phys.* **2014**, *47*, 405002.

(16) Zhu, K.; Chen, J.; Fan, Q.; Wang, L.; Xu, Q. Magnetoresistance of $(CH_3NH_3)PbI_3$-Coated $La_{0.67}Sr_{0.33}MnO_3$ Granular Composites. *IEEE Trans. Magn.* **2015**, *51*, 1−4.

(17) Wang, K.; Yang, Q.; Duan, J.; Zhang, C.; Zhao, F.; Yu, H.; Hu, B. Spin-Polarized Electronic Transport through Ferromagnet/Organic−Inorganic Hybrid Perovskite Spinterfaces at Room Temperature. *Adv. Mater. Interfaces* **2019**, *6*, 1900718.

(18) Wang, J.; Zhang, C.; Liu, H.; Liu, X.; Guo, H.; Sun, D.; Vardeny, Z. V. Tunable Spin Characteristic Properties in Spin Valve Devices Based on Hybrid Organic−Inorganic Perovskites. *Adv. Mater.* **2019**, *31*, 1904059.

(19) Wang, H.; Lei, J.; Gao, F.; Yang, Z.; Yang, D.; Jiang, J.; Li, J.; Hu, X.; Ren, X.; Liu, B. Magnetic Field-Assisted Perovskite Film

Preparation for Enhanced Performance of Solar Cells. *ACS Appl. Mater. Interfaces* **2017**, *9*, 21756.
(20) Zhang, C.; Sun, D.; Sheng, C. X.; Zhai, Y. X.; Mielczarek, K.; Zakhidov, A.; Vardeny, Z. V. Magnetic Field Effects in Hybrid Perovskite Devices. *Nat. Phys.* **2015**, *11*, 427−434.
(21) Li, W.; Yuan, S.; Zhan, Y.; Ding, B. Tuning Magneto-Photocurrent between Positive and Negative Polarities in Perovskite Solar Cells. *J. Phys. Chem. C* **2017**, *121*, 9537−9542.
(22) Uspenskii, Y.; Kulatov, E.; Mariette, H.; Nakayama, H.; Ohta, H. Ab Initio Study of the Magnetism in GaAs, GaN, ZnO, and ZnTe-Based Diluted Magnetic Semiconductors. *J. Magn. Magn. Mater.* **2003**, *258−259*, 248−250.
(23) Xing, G. Z.; Yi, J. B.; Tao, J. G.; Liu, T.; Wong, L. M.; Zhang, Z.; Li, G. P.; Wang, S. J.; Ding, J.; Sum, T. C.; Huan, C. H. A.; Wu, T. Comparative Study of Room-Temperature Ferromagnetism in Cu-Doped ZnO Nanowires Enhanced by Structural Inhomogeneity. *Adv. Mater.* **2008**, *20*, 3521−3527.
(24) Li, Y.; Deng, R.; Tian, Y.; Yao, B.; Wu, T. Role of Donor-Acceptor Complexes and Impurity Band in Stabilizing Ferromagnetic Order in Cu-doped $SnO_2$ Thin Films. *Appl. Phys. Lett.* **2012**, *100*, 172402.
(25) Yan, H.; Zhang, Z.; Wang, S.; Zhang, H.; Chen, C.; Jin, K. Modulated Transport Behavior of Two-Dimensional Electron Gas at Ni-Doped $LaAlO_3/SrTiO_3$ Heterointerfaces. *ACS Appl. Mater. Interfaces* **2017**, *9*, 39011−39017.
(26) Zhou, L.; Wiebe, J.; Lounis, S.; Vedmedenko, E.; Meier, F.; Blügel, S.; Dederichs, P. H.; Wiesendanger, R. Strength and Directionality of Surface Ruderman−Kittel−Kasuya−Yosida Interaction Mapped on the Atomic Scale. *Nat. Phys.* **2010**, *6*, 187−191.
(27) Zhao, Y. J.; Shishidou, T.; Freeman, A. J. Ruderman-Kittel-Kasuya-Yosida−like Ferromagnetism in $Mn_xGe_{1-x}$. *Phys. Rev. Lett.* **2003**, *90*, No. 047204.
(28) Anderson, P. W. Antiferromagnetism. Theory of Superexchange Interaction. *Phys. Rev.* **1950**, *79*, 350−356.
(29) Zener, C. Interaction Between the d-Shells in the Transition Metals. II. Ferromagnetic Compounds of Manganese with Perovskite Structure. *Phys. Rev.* **1951**, *82*, 403.
(30) Williams, S. T.; Rajagopal, A.; Jo, S. B.; Chueh, C. C.; Tang, T. F. L.; Kraeger, A.; Jen, A. K. Y. Realizing a New Class of Hybrid Organic−Inorganic Multifunctional Perovskite. *J. Mater. Chem. A* **2017**, *5*, 10640−10650.
(31) Klug, M. T.; Osherov, A.; Haghighirad, A. A.; Stranks, S. D.; Brown, P. R.; Bai, S.; Wang, J. T. W.; Dang, X.; Bulović, V.; Snaith, H. J.; Belcher, A. M. Tailoring Metal Halide Perovskites Through Metal Substitution: Influence on Photovoltaic and Material Properties. *Energy Environ. Sci.* **2017**, *10*, 236−246.
(32) Nafradi, B.; Szirmai, P.; Spina, M.; Lee, H.; Yazyev, O. V.; Arakcheeva, A.; Chernyshov, D.; Gibert, M.; Forro, L.; Horvath, E. Optically Switched Magnetism in Photovoltaic Perovskite $CH_3NH_3(Mn:Pb)I_3$. *Nat. Commun.* **2016**, *7*, 13406.
(33) Cai, B.; Chen, X.; Xie, M.; Zhang, S.; Liu, X.; Yang, J.; Zhou, W.; Guo, S.; Zeng, H. A Class of Pb-Free Double Perovskite Halide Semiconductors with Intrinsic Ferromagnetism, Large Spin Splitting and High Curie Temperature. *Mater. Horiz.* **2018**, *5*, 961−968.
(34) Yang, J. K.; Kim, W. S.; Park, H. H. Chemical Bonding States and Energy Band Gap of $SiO_2$ -Incorporated $La_2O_3$ Films on n-GaAs (001). *Thin Solid Films* **2006**, *494*, 311−314.
(35) Zhang, Z.; Ren, L.; Yan, H.; Guo, S.; Wang, S.; Wang, M.; Jin, K. Bandgap Narrowing in Bi-Doped $CH_3NH_3PbCl_3$ Perovskite Single Crystals and Thin Films. *J. Phys. Chem. C* **2017**, *121*, 17436−17441.
(36) Butler, K.; Frost, J.; Walsh, A. Band Alignment of the Hybrid Halide Perovskites $CH_3NH_3PbCl_3$, $CH_3NH_3PbBr_3$ and $CH_3NH_3PbI_3$. *Mater. Horiz.* **2015**, *2*, 228−231.
(37) Li, W.; Zhang, C.; Ma, Y.; Liu, C.; Fan, J.; Mai, Y.; Schropp, R. E. I. In Situ Induced Core/Shell Stabilized Hybrid Perovskites via Gallium(iii) Acetylacetonate Intermediate towards Highly Efficient and Stable Solar Cells. *Energy Environ. Sci.* **2018**, *11*, 286−293.
(38) Dietl, T. A Ten-Year Perspective on Dilute Magnetic Semiconductors and Oxides. *Nat. Mater.* **2010**, *9*, 965−974.
(39) Fukumura, T.; Jin, Z.; Ohtomo, A.; Koinuma, H.; Kawasaki, M. An Oxide-Diluted Magnetic Semiconductor: Mn-Doped ZnO. *Appl. Phys. Lett.* **1999**, *75*, 3366.
(40) Hsieh, T. Y.; Huang, C. K.; Su, T. S.; Hong, C. Y.; Wei, T. C. Crystal Growth and Dissolution of Methylammonium Lead Iodide Perovskite in Sequential Deposition: Correlation between Morphology Evolution and Photovoltaic Performance. *ACS Appl. Mater. Interfaces* **2017**, *9*, 8623−8633.
(41) Cheng, C.-J.; Lu, C.; Chen, Z.; You, L.; Chen, L.; Wang, J.; Wu, T. Thickness-Dependent Magnetism and Spin-Glass Behaviors in Compressively Strained $BiFeO_3$ Thin Films. *Appl. Phys. Lett.* **2011**, *98*, 242502.
(42) Story, T.; Galazka, R. R.; Frankel, R. B.; Wolff, P. A. Carrier-Concentration-Induced Ferromagnetism in PbSnMnTe. *Phys. Rev. Lett.* **1986**, *56*, 777−779.
(43) Black-Schaffer, A. M. RKKY Coupling in Graphene. *Phys. Rev. B: Condens. Matter Mater. Phys.* **2010**, *81*, 205416.
(44) Saidaminov, M. I.; Abdelhady, A. L.; Murali, B.; Alarousu, E.; Burlakov, V. M.; Peng, W.; Dursun, I.; Wang, L.; He, Y.; Maculan, G.; Goriely, A.; Wu, T.; Mohammed, O. F.; Bakr, O. M. High-Quality Bulk Hybrid Perovskite Single Crystals within Minutes by Inverse Temperature Crystallization. *Nat. Commun.* **2015**, *6*, 7586.
(45) Yu, W.; Li, F.; Yu, L.; Niazi, M. R.; Zou, Y.; Corzo, D.; Basu, A.; Ma, C.; Dey, S.; Tietze, M. L.; Buttner, U.; Wang, X.; Wang, Z.; Hedhili, M. N.; Guo, C.; Wu, T.; Amassian, A. Single Crystal Hybrid Perovskite Field-Effect Transistors. *Nat. Commun.* **2018**, *9*, 5354.
(46) Guo, H. Z.; Burgess, J.; Ada, E.; Street, S.; Gupta, A.; Iliev, M. N.; Kellock, A. J.; Magen, C.; Varela, M.; Pennycook, S. J. Influence of Defects on Structural and Magnetic Properties of Multifunctional $La_2NiMnO_6$ thin films. *Phys. Rev. B: Condens. Matter Mater. Phys.* **2008**, *77*, 174423.
(47) Oku, M.; Hirokawa, K.; Ikeda, S. X-ray Photoelectron Spectroscopy of Manganese-Oxygen Systems. *J. Electron Spectrosc. Relat. Phenom.* **1975**, *7*, 465−473.
(48) Oku, M.; Hirokawa, K. X-ray Photoelectron Spectroscopy of Co3O4, Fe3O4, Mn3O4, and Related Compounds. *J. Electron Spectrosc. Relat. Phenom.* **1976**, *8*, 475−481.
(49) Kowalczyk, S. P.; Ley, L.; Mcfeely, F. R.; Shirley, D. A. Multiplet Splitting of the Manganese and Levels in Mn Single Crystals. *Phys. Rev. B* **1975**, *11*, 1721−1727.
(50) Nesbitt, H.; Banerjee, D. Interpretation of XPS Mn (2p) Spectra of Mn Oxyhydroxides and Constraints on the Mechanism of $MnO_2$ Precipitation. *Am. Mineral.* **1998**, *83*, 305−315.
(51) Grissa, R.; Martinez, H.; Cotte, S.; Galipaud, J.; Pecquenard, B.; Le Cras, F. Thorough XPS Analyses on Overlithiated Manganese Spinel Cycled around the 3V Plateau. *Appl. Surf. Sci.* **2017**, *411*, 449−456.
(52) Lourembam, J.; Wu, J.; Ding, J.; Lin, W.; Wu, T. Electric Field Tuning of Phase Separation in Manganite Thin Films. *Phys. Rev. B: Condens. Matter Mater. Phys.* **2014**, *89*, No. 014425.
(53) Wu, T.; Ogale, S. B.; Garrison, J. E.; Nagaraj, B.; Biswas, A.; Chen, Z.; Greene, R. L.; Ramesh, R.; Venkatesan, T.; Millis, A. J. Electroresistance and Electronic Phase Separation in Mixed-Valent Manganites. *Phys. Rev. Lett.* **2001**, *86*, 5998−6001.
(54) Zener, C. Interaction Between the d Shells in the Transition Metals. *Phys. Rev.* **1951**, *81*, 440.
(55) Warner, J. W.; Berry, R. S. *Nature* **1985**, *313*, 160−160.
(56) Kataoka, T.; Yamazaki, Y.; Singh, V. R.; Fujimori, A.; Chang, F. H.; Lin, H. J.; Huang, D. J.; Chen, C. T.; Xing, G. Z.; Seo, J. W.; Panagopoulos, C.; Wu, T. Ferromagnetic Interaction between Cu Ions in the Bulk Region of Cu-doped ZnO Nanowires. *Phys. Rev. B: Condens. Matter Mater. Phys.* **2011**, *84*, 153203.
(57) Finck, B. Y.; Schwartz, B. J. Understanding the Origin of the S-curve in Conjugated Polymer/Fullerene Photovoltaics from Drift-Diffusion Simulations. *Appl. Phys. Lett.* **2013**, *103*, No. 053306.
(58) Roy, S.; Ali, N. Charge Transport and Colossal Magnetoresistance Phenomenon in $La_{1-x}Zr_xMnO_3$. *J. Appl. Phys.* **2001**, *89*, 7425−7427.


https://dx.doi.org/10.1021/acs.jpclett.0c00034
J. Phys. Chem. Lett. 2020, 11, 2577−2584

(59) Kormondy, K. J.; Gao, L.; Li, X.; Lu, S.; Posadas, A. B.; Shen, S.; Tsoi, M.; Mccartney, M. R.; Smith, D. J.; Zhou, J.; et al. Large Positive Linear Magnetoresistance in the Two-Dimensional $t_{2g}$ Electron Gas at the EuO/$SrTiO_3$ Interface. *Sci. Rep.* **2018**, *8*, 7721.

(60) David, A.; Tian, Y.; Yang, P.; Gao, X.; Lin, W.; Shah, A. B.; Zuo, J. M.; Prellier, W.; Wu, T. Colossal positive magnetoresistance in surface-passivated oxygen-deficient strontium titanite. *Sci. Rep.* **2015**, *5*, 10255.



https://dx.doi.org/10.1021/acs.jpclett.0c00034
*J. Phys. Chem. Lett.* 2020, 11, 2577−2584